Journal of Solid State Chemistry **160,** 368–376 (2001)
doi:10.1006/jssc.2001.9242, available online at http://www.idealibrary.com on IDEAL®

NMR and FT-IR Investigation of Spinel $LiMn_2O_4$ Cathode Prepared by the Tartaric Acid Gel Process

Y. M. Hon, H. Y. Chung, K. Z. Fung,[1] and M. H. Hon

Department of Materials Science and Engineering, National Cheng Kung University, Tainan 70101, Taiwan

Received January 23, 2001; in revised form May 2, 2001; accepted May 11, 2001; published online June 29, 2001

The structure of the lithium manganese tartrate precursor and the synthesis mechanism of $LiMn_2O_4$ were investigated by FT-IR, NMR, TG/DSC, and XRD in this study. The results of FT-IR and ^7Li and ^{13}C NMR measurements revealed that lithium ions bond with carboxylic acid ligands and the O–H stretching modes of tartaric acid. Manganese ion bonds only with carboxylic acid. Lithium and manganese ions were trapped homogeneously on an atomic scale throughout the precursor. Such a structure eliminates the need for long-range diffusion during the formation of lithium manganese oxides. Therefore, spinel $LiMn_2O_4$ was synthesized at temperatures as low as 300°C. In this work, the electrochemical properties of $Li/Li_xMn_2O_4$ were studied. It is clear that the discharge curves exhibit two pseudo plateaus as the $LiMn_2O_4$ is fired to higher temperatures. The discharge capacity of $LiMn_2O_4$ increases from 84 to 117 mAh/g as the calcination temperature increases from 300 to 500°C. The $LiMn_2O_4$ powders calcined at low temperatures with a high specific surface area and an average valence of manganese exhibit a better cycle life.

Key Words: **lithium manganese oxide; tartaric acid; cathode materials; lithium ion battery.**

I. INTRODUCTION

Layered oxides $LiCoO_2$, $LiNiO_2$, and the cubic spinel $LiMn_2O_4$ have been widely studied as cathodes in 4-V rechargeable Li cells. Among them, the spinel $LiMn_2O_4$ is a particularly attractive cathode material for commercial lithium ion batteries, because of its low cost and lower toxicity compared with the layered oxides $LiCoO_2$ and $LiNiO_2$ (1). However, the cyclability of $LiMn_2O_4$ in 4-V cell is inferior to that of the layered oxides. Several degradation mechanisms have been proposed such as (a) structural damage due to Jahn–Teller distortion, (b) dissolution of the spinel into the electrolyte, and (c) oxidation of the electrolyte on the surface of the cathode at a high charge state (2). It is well known that there exists a wide range of solid solutions in the Li–Mn–O spinel system. Recently, it was reported that the potential and electrochemical properties of the $Li_{1-x}Mn_2O_4$ cathode are strongly dependent on the synthesis method, calcination temperature, and cooling rate (3–5).

The synthesis of $LiMn_2O_4$ is generally categorized into two methods: a solid-state method and solution method. The conventional solid-state method for $LiMn_2O_4$ involves the mechanical mixing of starting materials, followed by long-term high-temperature treatment and extended grinding. Usually, the synthesis of spinel $LiMn_2O_4$ phase using solid-state reactions requires temperatures as high as 700°C (6). Moreover, the final product from solid-state reaction usually contains impure phases, irregular morphology, larger particle size, and broader particle size distribution. High calcination temperatures and repeated long-term annealing may also affect the cycling properties of the $LiMn_2O_4$ electrode. For the battery application, it is believed that electrode materials with a single phase, high purity, uniform particle size distribution, and high surface area are considered to be required for better performance of the electrodes (7, 8). In additions, the low lithium ion mobility and the Jahn–Teller distortion also pose some difficulties in the development of a $LiMn_2O_4$ cathode. One way to minimize the problem of Li ion mobility is to keep the particle size of $LiMn_2O_4$ small and thereby reduce the diffusion length of Li ions.

Several techniques, such as sol–gel (9), coprecipitation (10), melt impregnation (11), the citric acid method (12, 13), the tartaric acid method (14, 15), and the Pechini process (16), have been developed. $LiMn_2O_4$ powder synthesis by the tartaric acid gel process using lithium acetate and manganese acetate as the lithium and manganese sources has been shown to be an inexpensive method with great potential. Although $LiMn_2O_4$ has been successfully synthesized by the tartaric acid gel process, the structure of lithium manganese tartrate precursor and the synthesis mechanism of lithium manganese oxide are not fully understood.

In addition, solution synthesis of the $LiMn_2O_4$ precursor is often hindered by the high solubility of lithium salts in

[1] To whom correspondence should be addressed. Fax: 886-6-2380208. E-mail: kzfung@mail.ncku.edu.tw.

0022-4596/01 $35.00

water or ethanol. Thus, attaining good stoichiometric control of the Li:Mn ratio in the end product is a big challenge. When tartaric acid is added to the precursor to chelate the metal ions, whether the lithium ion bonds with the COOH– or OH of tartaric acid or just absorbs physically on the surface of the precursor has not been determined.

In this paper, FT-IR, NMR, XRD, and DSC/TG methods were used to study the structure of the lithium manganese tartrate precursor and the synthesis mechanism of lithium manganese oxide by the tartaric acid gel process. The electrochemical properties of $LiMn_2O_4$ powders calcined at 300–500°C were also studied.

II. EXPERIMENTAL PROCEDURE

II.1. Precursors Formed by the Tartaric Acid Gel Process

Lithium acetate (98% purity, Aldrich) and manganese acetate (99% purity, Showa Chemicals Inc.) used as sources for lithium and manganese were dissolved in ethanol, the molar ratio of metal ions Li^+:Mn^{2+} being controlled at 1:2. The metal ion ethanol solution was then mixed with the ethanol solution of tartaric acid (99.5% purity, Katayama). During mixing, the solution abruptly transformed into a viscous gel. The final gel contained 0.025 M Li^+, 0.05 M Mn^{2+}, and 0.1 M tartaric acid. The gel was subsequently heated in an oven at 68°C to remove the ethanol. After drying, the lithium manganese tartrate precursor became a hard agglomerate with a pinkish color.

II.2. Calcination Process

The precursor was then heated at 200°C for 6 h to slowly remove the moisture. Subsequently the calcination process was conducted at temperatures ranging from 265 to 500°C for 24 h in air. Finally, the calcined powders were furnace-cooled to room temperature for further investigation.

II.3. NMR, Thermal Analysis, and FT-IR Investigation

Solid-state ^{7}Li NMR spectra were obtained using a Bruker AVANCE 400 spectrometer. ^{7}Li spectra were acquired at 155.5 MHz, using the spin–echo method, a recycling delay of 1 s, and a 90° pulse width for ^{7}Li of 3.3 μs. All spectra were referenced to an external $LiCl_{(aq)}$ standard.

Thermal analysis was carried out using a differential scanning calorimeter (DSC, Netzsch 404) and thermogravimetric analysis (TG, TA2950) to investigate the possible phase transformations between 25 and 1000°C with a heating rate of 5°C/min in air. A Fourier transform infrared spectrometer (FT-IR, JASCO FT/IR-410) was used to study the structure coordination of the precursors. Each sample was mixed with KBr and examined in the wavenumber range from 400–4000 cm^{-1}.

II.4. Crystallographic and Chemical Analysis

The phase identity, crystal structure, and lattice constants of the materials were investigated by using a Rigaku X-ray diffractometer (XRD) with Cu$K\alpha$ radiation at 30 kV, 20 mA. XRD data collected between 10–70° of 2θ angles with a step interval of 0.01° and a scanning rate of 1°/min. Lattice constants were determined by a least-squares refinement of the *d*-spacings, which were measured in comparison with an internal standard of pure Si. The concentration of lithium and manganese in the samples calcined at various temperatures was analyzed by using inductively coupled plasma (ICP, Janell-Ash, ICAP 9000). The average valence of manganese was determined by the titration method. About 0.06 g of the sample was dissolved in 20 ml of an acidified 0.08 M Fe(II) solution. During dissolution higher Mn oxidation states (III and IV) are reduced to Mn(II) by the oxidation of Fe(II) to Fe(III). The excess Fe(II) was back-titrated with 0.018 M $KMnO_4$.

II.5. Morphology and Specific Surface Area Characterization

A scanning electron microscope (SEM, Philips XL-40FEG) was used to examine the particle size and morphology of the synthesized powders. The specific surface area of lithium manganese oxide powders was measured by using a GEMINI 2360 surface area analyzer based on the BET process.

II.6. Electrochemical Properties

The two-electrode cell was used for the charge–discharge experiment. The anode was constructed from the lithium foil (FMC). The electrolyte was a 1:1 (v/v) mixture of ethylene carbonate (EC) and diethyl carbonate (DEC) containing 1 M $LiPF_6$ (Mitsubishi Chemical). The cathode contained 70% active material, 17% KS-6 carbon black, and 13% PVDF binder. The cell was assembled in an argon-filled drybox. Charge–discharge cycling was performed at a current density of 0.1 mA/cm^2, with a cut-off voltage of 3.0 to 4.3 V (vs Li/Li^+).

III. RESULTS AND DISCUSSION

III.1. Structure of Lithium Manganese Tartrate Precursor

(i) FT-IR analysis. Figure 1a shows the FT-IR spectra of tartaric acid. The broad IR band located at 3317 cm^{-1} is attributed to the O–H streching vibration in tartaric acid. Bands corresponding to carboxylate anion were observed at 1740, 1625, and 1340 cm^{-1}. Similar experiments were also conducted on lithium tartrate, manganese tartrate, and lithium manganese tartrate precursors.

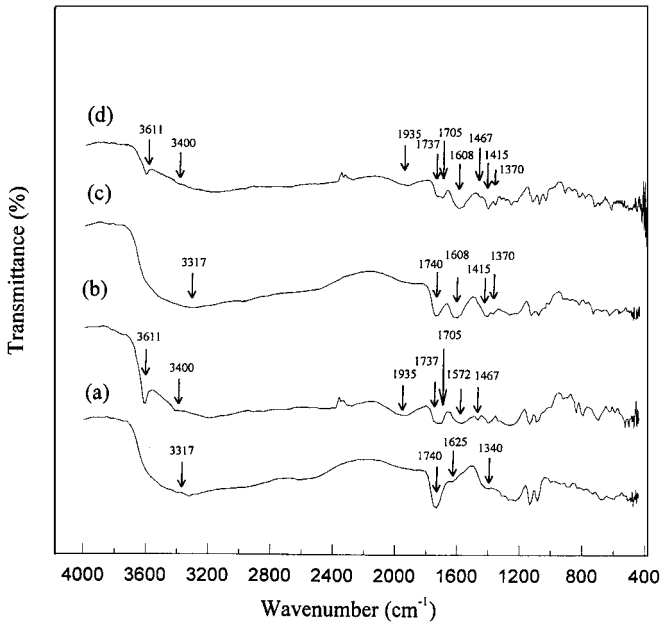

FIG. 1. FT-IR spectra of (a) tartaric acid, (b) lithium tartrate, (c) manganese tartrate, and (d) lithium manganese tartrate precursors.

In FT-IR spectra for lithium tartrate and lithium manganese tartrate precursors, the difference in the O–H streching vibration from tartaric acid was observed. However, the IR analysis conducted on manganese tartrate precursor showed nearly the same IR spectra as tartaric acid at wavenumber near 3317 cm^{-1}. The broad IR band at 3317 cm^{-1} from tartaric acid split into two peaks at 3611 and 3400 cm^{-1} when the lithium compound was formed. This result suggests that lithium ions bond with the O–H streching vibration, which causes the splitting of IR spectra at wavenumber near 3317 cm^{-1}. However, it was found that manganese ions bond only with carboxylate anion without bonding with the O–H streching vibration. These results are consistent with the NMR spectroscopy results that are discussed in a later section.

(ii) NMR analysis. Solid-state NMR is known to provide information concerning the coordination and composition of solid materials (17). In this study, solid-state ^{13}C NMR was used to study both tartaric acid and lithium tartrate precursors. Figure 2 shows ^{13}C NMR spectra of tartaric acid and lithium tartrate at 25°C. For tartaric acid, peaks are located at 176.6 and 171.9 ppm, representing the alcoholic carbon (HO–C–). Also, peaks at 74.6 and 72.3 ppm originate from the carboxylic acid group (HOO–C) in tartaric acid. However, double peaks representing the carboxylic acid group for tartaric acid split into four peaks at 73.5, 72.9, 72.76, and 72.2 ppm for lithium tartrate precursors. Peaks representing the alcoholic carbon are also split into four peaks at 181.6, 179.9, 178.8, and 178.5 ppm. The peak splitting indicates that a proton was dissociated from the alcoholic OH group. Subsequently, the deprotonated alcoholic ligand was coordinated with the lithium ion.

In addition, ^{7}Li NMR spectra were also used to study the bonding environment. Figure 3 shows the ^{7}Li NMR spectra of the lithium tartrate precursor at a spinning speed of 6 kHz. The peaks at 0.99 ppm correspond to the new band formation between the lithium ion and the carboxylic acid ligand. Similarly, the peaks at -0.6 ppm arise from the new bond formation between the lithium ion and the deprotonated alcoholic ligand.

On the basis of the FT-IR and ^{13}C and ^{7}Li NMR spectra, the structure of lithium manganese tartrate precursor is proposed as shown in Fig. 4. As can be seen from the figure, lithium and manganese are homogeneously coordinated on an atomic scale throughout the precursor structure. Thus, $LiMn_2O_4$ powder can be synthesized at low temperatures by the tartaric acid gel process.

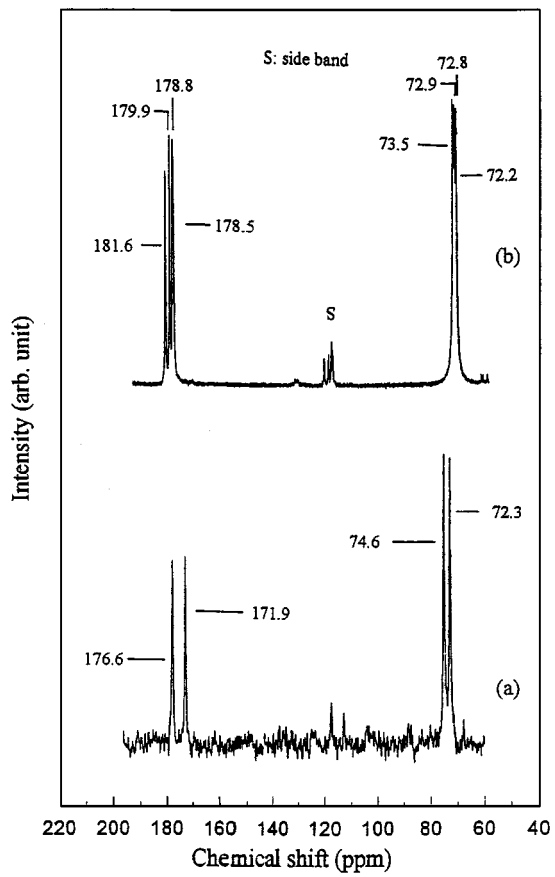

FIG. 2. ^{13}C NMR spectra of (a) tartaric acid and (b) lithium tartrate precursors.

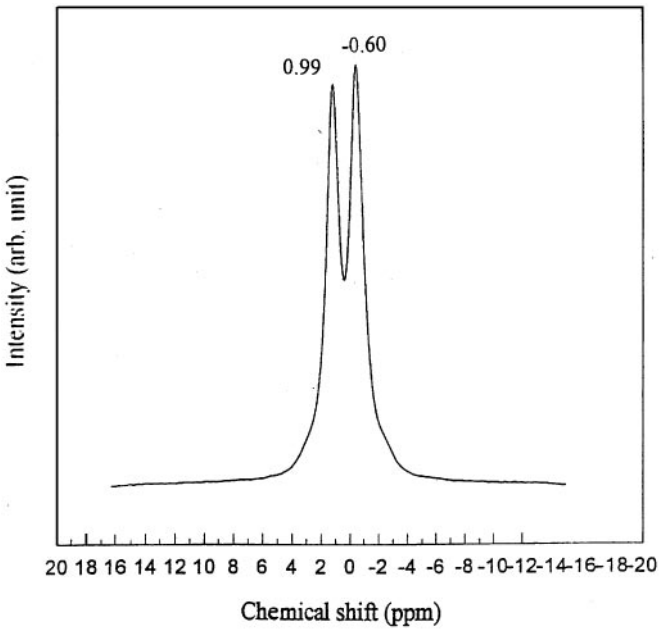

FIG. 3. ^{7}Li NMR spectra of lithium tartrate precursor.

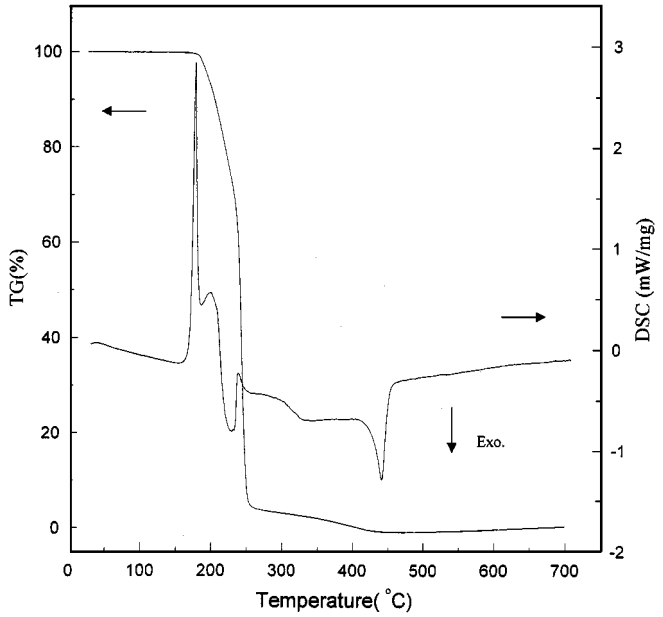

FIG. 5. TG/DSC analysis for tartaric acid at a heating rate of 5°C/min in air.

III.2. Synthesis Mechanism of $LiMn_2O_4$ by the Tartaric Acid Gel Process

As shown in Fig. 5, the TG/DSC analysis was first conducted on pure tartaric acid at a heating rate of 5°C/min. The TG curve shows a significant weight loss starting at about 190°C and continuing to about 250°C. Nearly 95 wt% loss was observed. The DSC curve shows two endothermic peaks and one exothermic peak between 150–250°C which correspond to the decomposition and combination of organic compound. The second weight loss at 440°C with an exothermic peak can be ascribed to combustion of tartaric acid derivations or residual carbon.

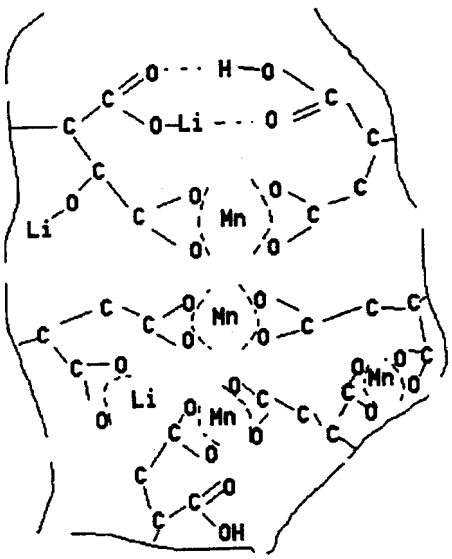

FIG. 4. Schematic illustration of the overall structure of the lithium manganese tartrate precursor.

In order to understand the decomposition behavior of the lithium manganese tartrate precursor thoroughly, lithium tartrate and manganese tartrate precursors were prepared individually and characterized by TG/DSC and/or XRD, respectively. The TG/DSC curves of lithium tartrate precursor are shown in Fig. 6. The figure shows the abrupt weight loss between 150–250°C as well as one endothermic peak at 176°C and one exothermic peak at 232°C. As temperature increased, a strong exothermic peak was obtained at 610°C. This exothermic reaction is attributed to the combustion of tartaric acid derivations or residual carbon. In order to determine the phase(s) formed at various temperatures, X-ray diffraction studies were conducted. Figure 7 shows the XRD traces of lithium tartrate precursors, which were calcined at 400, 600, and 700°C, respectively, for 20 min. X-ray diffraction analysis indicates that the major phase in all samples was Li_2CO_3. In comparison with the results of TG/DSC and XRD for the lithium tartrate precursor it may be concluded that the exothermic peak at 222°C corresponds to the formation of Li_2CO_3.

Figure 8 shows the TG/DSC curves for manganese tartrate precursors. The TG curve shows weight loss starting at

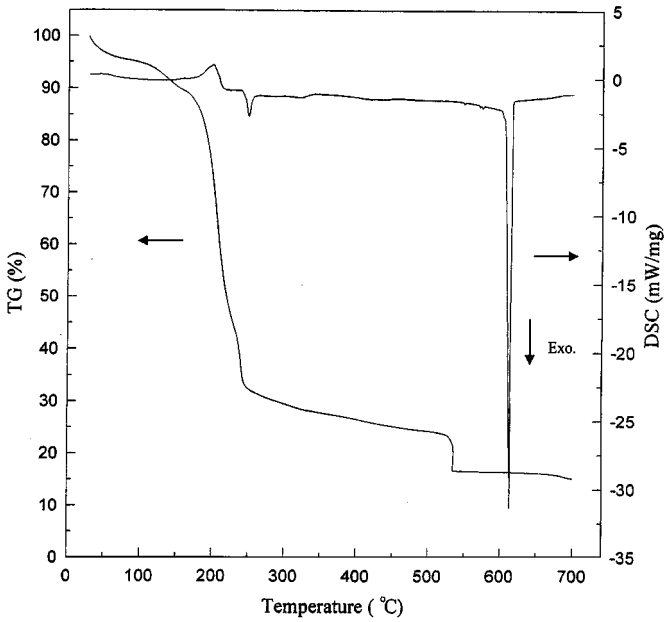

FIG. 6. TG/DSC analysis for lithium tartrate precursor at a heating rate of 5°C/min in air.

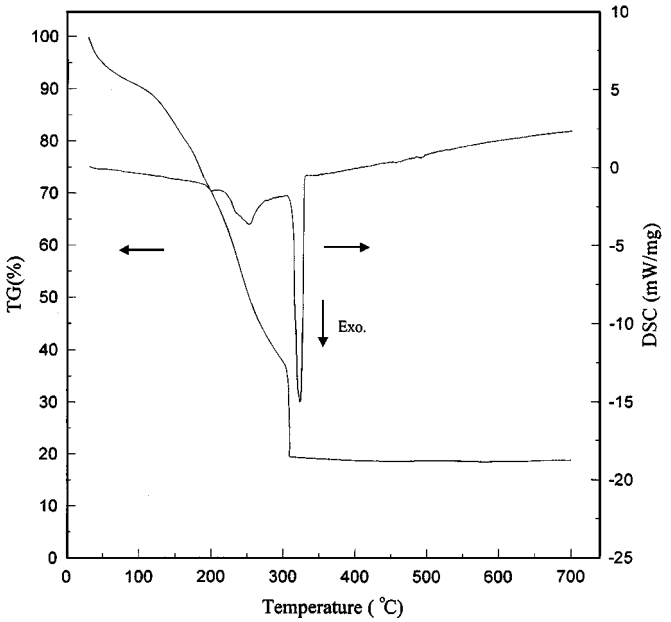

FIG. 8. TG/DSC analysis for manganese tartrate precursor at a heating rate of 5°C/min in air.

room temperature and continuing to about 300°C. Nearly 80 wt% weight loss was measured. There are two exothermic reactions at 250 and 322°C. Figure 9 shows the XRD traces of manganese tartrate precursors, which were calcined at 290 and 340°C, respectively, for 20 min. The XRD patterns of manganese tartrate precursor calcined at 290 and 340°C were found to be those of manganese tartrate ($C_4H_4MnO_6$) and γ-Mn_3O_4, respectively. On the basis of the results of TG/DSC and XRD studies of the manganese tartrate precursor, the exothermic reaction at 250°C is

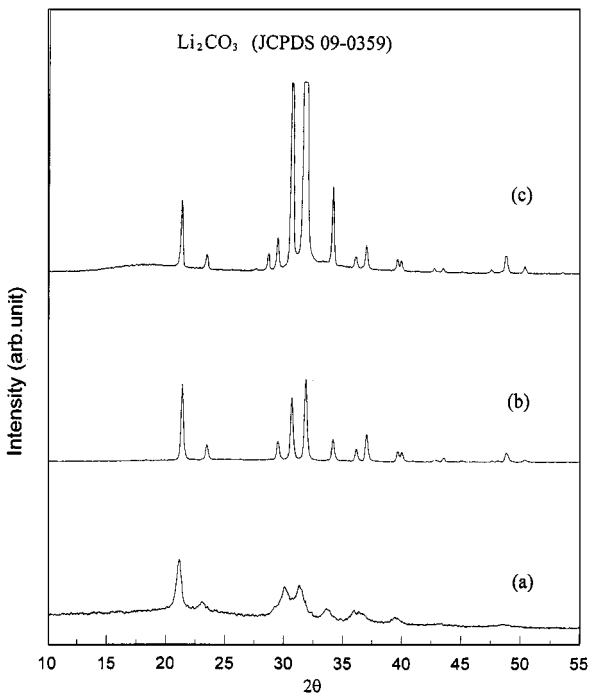

FIG. 7. XRD pattern of lithium tartrate precursor calcined at (a) 400°C, (b) 600°C, and (c) 700°C for 20 min.

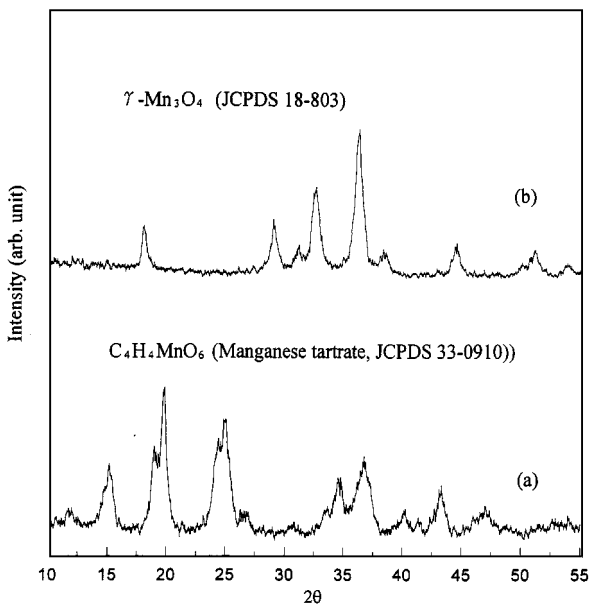

FIG. 9. XRD pattern of manganese tartrate precursor calcined at (a) 290°C and (b) 340°C for 20 min.

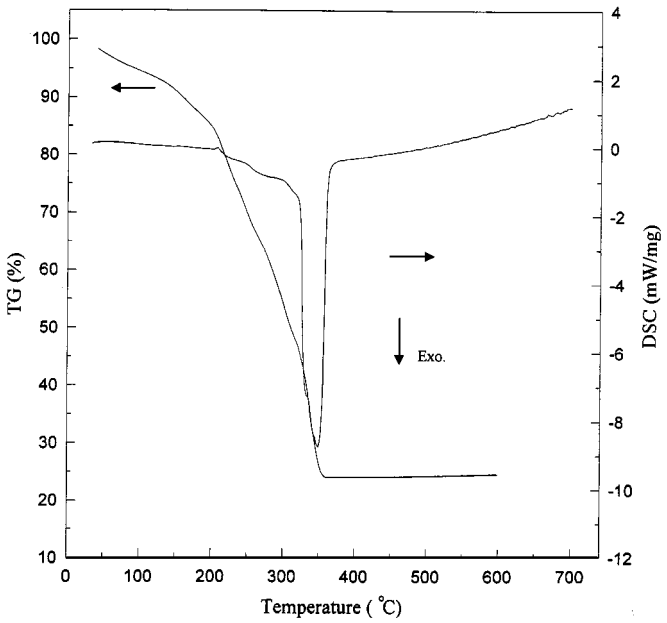

FIG. 10. TG/DSC analysis for lithium manganese tartrate precursor at a heating rate of 5°C/min in air.

attributed to the formation of manganese tartrate and another exothermic reaction at 322°C is accompanied by the formation of γ-Mn_3O_4.

Figure 10 shows the TG and DSC curves for the lithium manganese tartrate precursor. The TG curve shows three weight losses that can be divided into three temperature ranges: 25–150°C, 150–300°C, and 300–360°C. The first weight loss is due to the removal of water. The second weight loss is attributed to the decomposition of tartaric acid and acetate ions. The abrupt weight loss in the temperature range of 300–360°C with a huge exothermic reaction indicates the decomposition of organic in the precursor complex. There are one broad exothermal peak between 200–300°C, and there are two sharp exothermal peaks at 337 and 350°C. Figure 11 shows the XRD pattern of the lithium manganese precursor calcined at 290°C for various periods of time. X-ray diffraction analysis indicates that the $LiMn_2O_4$ with spinel structure was formed at 290°C without any second phase present.

We know that the tartaric acid not only functioned as a chelating agent but also released the heat during combustion, which enhanced the synthesis of lithium manganese oxide. When the lithium and manganese ions are trapped inhomogeneously on an atomic scale and aggregate in the precursor, the Li_2CO_3 and manganese tartrate may form at low temperatures. From the results of TG/DSC and XRD, it is believed that the lithium and manganese ions are trapped homogeneously on an atomic scale in the precursor. So, the $LiMn_2O_4$ forms immediately when the heat is released from the organic materials.

The XRD patterns of the lithium manganese tartrate precursor calcined at various temperatures for 24 h in air are shown in Fig. 12. For the sample calcined at 300°C, the crystallinity of the $LiMn_2O_4$ spinel phase was poor, but the impurities, including Li_2CO_3, MnO_2, and Mn_2O_3, were not observed. However, the peaks were relatively broad, presumably due to lattice strain in the spinel structure. The peaks gradually sharpened with increasing annealing temperature, which indicates an increase of crystallinity. Apparently, the lithium manganese tartrate precursor converted into the spinel $LiMn_2O_4$ without formation of minor or metastable phase in the calcination temperature ranges. These results strongly highlight that this tartaric acid gel method was highly superior to the solid-state reaction since pure spinel $LiMn_2O_4$ powders can be prepared at much lower calcination temperatures attributed to the shorter Li–Mn ion distance and atomic-scale metal ion distribution in the precursor.

The concentrations of Li and Mn and the average oxidation state of manganese in $LiMn_2O_4$ calcined at various temperatures are summarized in Table 1. The lattice constant increases from 8.157 to 8.196 Å as the calcination temperature increases from 300 to 500°C. The lattice parameters of the samples in this study were lower than those reported in the literature (18–21). Such a difference in lattice parameters may result from the lower calcination temperature in this study compared to the temperatures commonly used in the solid-state reaction method. When lithium manganese oxide was synthesized at low temperatures the

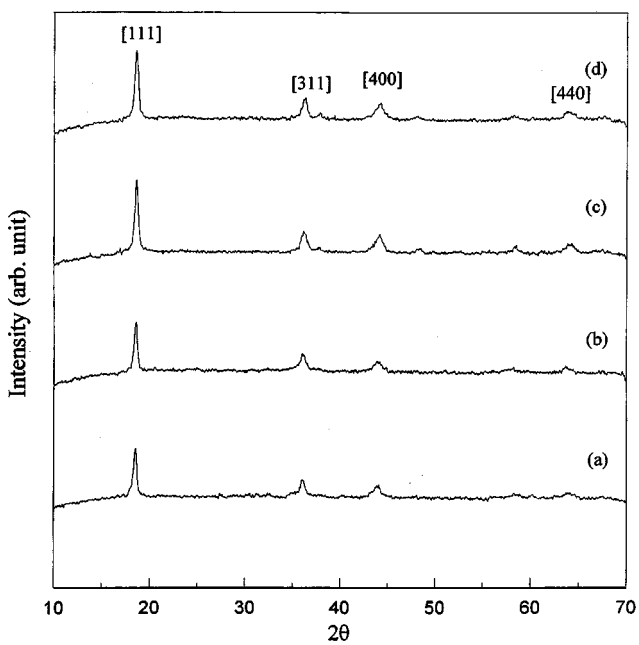

FIG. 11. XRD pattern of lithium manganese tartrate precursor calcined at 290°C for (a) 20, (b) 40, (c) 180, and (d) 360 min.

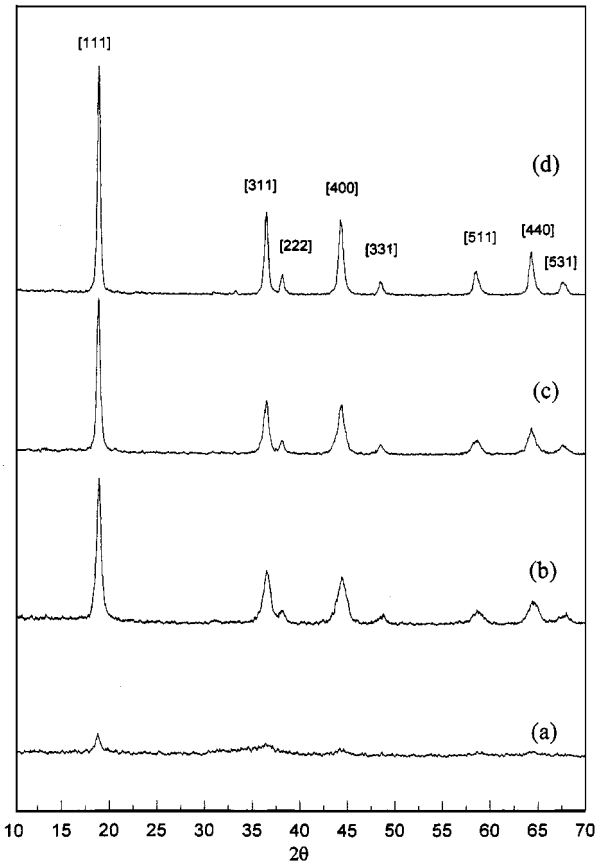

FIG. 12. XRD patterns of $LiMn_2O_4$ powders calcined at (a) 265°C, (b) 300°C, (c) 400°C, and (d) 500°C for 24 h.

cation-deficient structure was usually observed. The presence of vacancies in the cation sublattice tends to make the lattice smaller (13, 22). In addition, the spinel calcined at lower temperatures favors the formation of an oxidized manganese cation because manganese ions are stable preferentially as Mn^{4+} at lower temperatures (23, 24). Since the ionic radius of Mn^{4+} (0.67 Å) is smaller than that of Mn^{3+} (0.72 Å), the lattice constant of the spinel $LiMn_2O_4$ calcined at lower temperatures is expected to be smaller than that of the spinel calcined at higher temperatures.

III.3. Specific Surface Area and Morphology of Powders

The specific surface areas of powders calcined at various temperatures are shown in Table 1. The specific surface area of the powder calcined at 300°C was 55.5 m^2/g and quickly decreased to 28.4 m^2/g as the temperature increased to 400°C. This result is attributed to the large amount of heat released from the combustion of the precursor at about 350°C, which caused the agglomeration of fine particles.

Figure 13 shows the SEM micrographs of $LiMn_2O_4$ powders calcined at various temperatures. The average particle sizes of the powders increase from 20 to 40 nm as the calcination temperature increases from 300 to 500°C over 24 h. From the SEM results, the powders synthesized by the tartaric acid gel process showed a spherical shape and a narrow particle size distribution.

III.4. Electrochemical Properties

Figure 14 shows the fist discharge curves of $LiMn_2O_4$ calcined at 300, 400, and 500°C with a constant current density of 0.1 mA/cm^2 between cut-off voltages of 3.0 and 4.2 V. The $LiMn_2O_4$ powder calcined at 300°C did not show a distinct potential plateau. After $LiMn_2O_4$ was formed at 400 and 500°C, both discharge curves exhibited two pseudo plateaus with a separation of $\sim$120 mV, which is typical of the electrochemical extraction and insertion of Li in the stoichiometric spinel $LiMn_2O_4$.

This result indicates that the coulombic repulsive reaction is small, which may be attributed to lower crystallization of the sample calcined at low temperatures. These two plateau voltages of samples calcined at high temperatures correspond to a two-phase reaction. One possible interpretation is that in the first plateau region, lithium ions occupy every other available tetrahedral sites (8*a*) in the spinel structure, until half the sites are filled. At this point, the phase transformation from λ-MnO_2 to $Li_{0.5}Mn_2O_4$ is complete, producing single-phase $Li_{0.5}Mn_2O_4$ (25). In the second plateau region, lithium ions may fill the remaining 8*a* sites. This arrangement increases repulsion between the lithium ions, resulting in a small increase in the free energy in the system as reflected by the observed voltage drop. In the fully

TABLE 1
Lattice Parameters, Chemical Analyses and Specific Surface Areas of $LiMn_2O_4$ Powders

Temperature (°C)	Lattice parameter (*a*, Å)	Li (wt%)	Mn (wt%)	Average valence of Mn	Specific surface area (BET, m^2/g)
300	8.1569	3.57	55.0	3.63	55.5
400	8.1616	3.74	56.1	3.53	28.4
500	8.1961	3.67	56.2	3.52	23.0

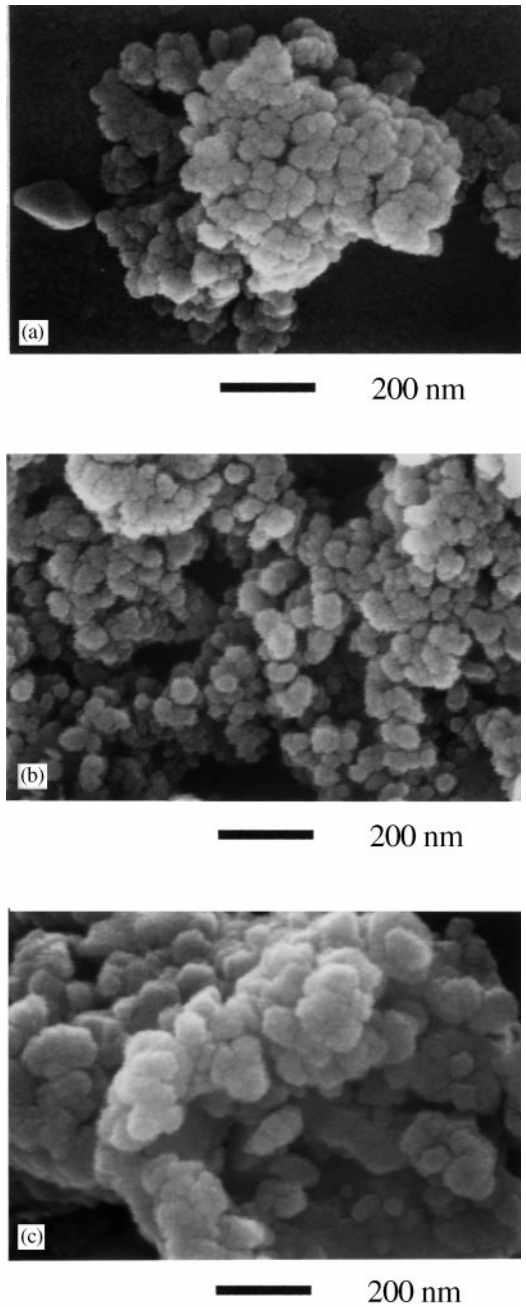

FIG. 13. SEM micrographs of $LiMn_2O_4$ powders prepared by the tartaric acid gel process at (a) 300°C, (b) 400°C, and (c) 500°C, for 24 h.

discharged state, the transformations from $Li_{0.5}Mn_2O_4$ to $LiMn_2O_4$ are complete. An increase in the firing temperature is believed to enhance the crystallization of the $LiMn_2O_4$ structure. Hence, a more distinct two-step electrochemical reaction was observed.

The discharge capacity of $LiMn_2O_4$ increases from 84 to 117 mAh/g as the calcination temperature increases from 300 to 500°C. The average valence of manganese in the

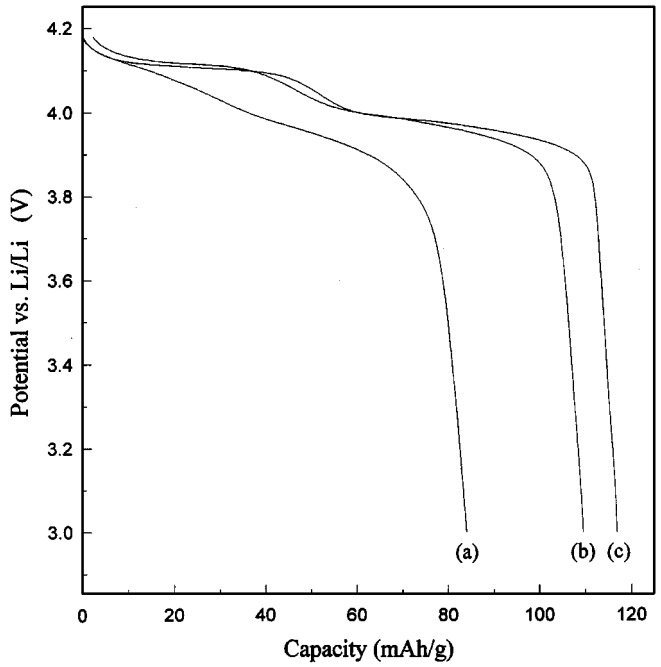

FIG. 14. Discharge curves of $LiMn_2O_4$ powders calcined at (a) 300°C, (b) 400°C, and (c) 500°C with a discharge current density of 0.1 mA/cm^2.

products decreases with an increase of the calcination temperature, as shown in Table 1. When the samples are synthesized at 500°C, the average valence of manganese

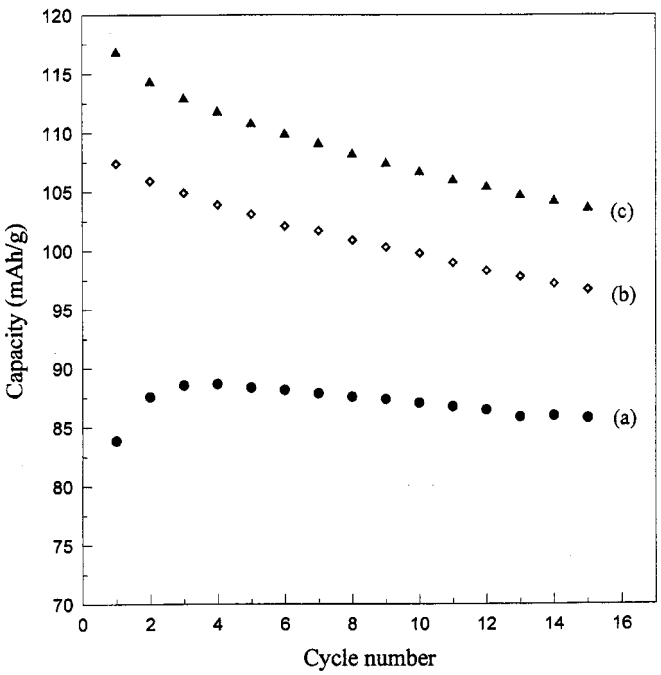

FIG. 15. Discharge capacity vs cycle number of $LiMn_2O_4$ powders calcined at (a) 300°C, (b) 400°C, and (c) 500°C with a current density of 0.1 mA/cm^2.

is close to 3.5, and the product has the highest specific capacity.

Figure 15 shows the discharge capacity with the cycle number for the $LiMn_2O_4$ powders calcined at 300, 400, and 500°C with a constant charge–discharge current density of 0.1 mA/cm^2. As the calcination temperature decreases, the initial discharge capacity decreases, but the cycling characteristic is improved. The $LiMn_2O_4$ powders calcined at 400 and 500°C delivered initial capacities of 107 and 117 mAh/g. After 15 cycles, the discharge capacity decreases to 92 and 89% of the initial capacity, respectively. However, the discharge capacity of the $LiMn_2O_4$ powder calcined at 300°C increases initially from 83.9 to 88.7 mAh/g and shows very stable capacity.

The lower initial capacity and better cycling behavior of $LiMn_2O_4$ powders calcined at 300°C are due to its low crystallinity and small particle size which enhance lithium ion diffusion and the intercalation–deintercalation process (26). In additions, the average valence of manganese for the powder calcined at 300°C was 3.63, which means fewer manganese ions were in the $+3$ state. The Mn^{3+} is in the high-spin state (one d electron in an e_g orbital), which is the main cause for the Jahn–Teller distortion during the intercalation–deintercalation process (27). Therefore, a lower extent of Jahn–Teller distortion occurred and a better cyclability was obtained.

IV. CONCLUSION

From the NMR and FT-IR results, the lithium ion not only bonded with the carboxylic acid (COO^-) ligand but also bonded with the O–H stretching modes in tartaric acid. But manganese ion only bonded with carboxylic acid. The lithium and manganese ions were trapped homogeneously on an atomic scale in the precursor. $LiMn_2O_4$ forms immediately when the heat is released from the organic materials. The specific surface area of the powder calcined at 300°C for 24 h was 55.5 m^2/g, which was apparently larger than that of the powder prepared by solid-state reaction. Therefore, $LiMn_2O_4$ powders with a spherical shape and a narrow particle size distribution can be synthesized by the tartaric acid gel process.

The $LiMn_2O_4$ powders calcined at 500°C delivered an initial capacity of 117 mAh/g. After 15 cycles, the discharge capacity decreased to 89% of the initial capacity. However, the discharge capacity of the $LiMn_2O_4$ powder calcined at 300°C increased initially from 83.9 to 88.7 mAh/g and showed a very stable capacity.

ACKNOWLEDGMENT

This work was financially supported by the National Science Council of Taiwan, Grant No. NSC 89-2216-E-006-052, which is gratefully acknowledged.

REFERENCES

1. D. Guyomard and J. M. Tarascon, *J. Electrochem. Soc.* **139,** 937 (1992).
2. G. X. Wang, D. H. Bradhurst, H. K. Liu, and S. X. Dou, *Solid State Ionics* **120,** 95 (1999).
3. Y. Gao and J. R. Dahn, *J. Electrochem. Soc.* **143,** 100 (1996).
4. J. M. Tarascon, W. R. McKinnon, F. Coowar, T. N. Bowmer, G. Amatucci, and D. Guyomard, *J. Electrochem. Soc.* **141,** 1421 (1994).
5. D. Aurbach, I. Weissman, H. Yamin, and E. Elster, *J. Electrochem. Soc.* **145,** 1421 (1998).
6. P. Endres, B. Fuchs, S. K. Sack, K. Brandt, G. F. Becker, and H. W. Praas, *Solid State Ionics* **89,** 221 (1996).
7. S. R. S. Prabaharan, N. B. Saparil, S. S. Michael, M. Massot, and C. Julien, *Solid State Ionics* **112,** 25 (1998).
8. L. Chen, X. Huang, E. Kelder, and J. Schoonman, *Solid State Ionics* **76,** 91 (1995).
9. S. Passerini, F. Coustier, M. Giorgetti, and W. H. Smyrl, *Electrochem. Solid-State Lett.* **2,** 483 (1999).
10. A. R. Naghash and J. Y. Lee, *J. Power Sources* **85,** 284 (2000).
11. Y. Xia, H. Takeshige, H. Noguchi, and M. Yoshio, *J. Power Sources* **56,** 61 (1995).
12. Y. M. Hon, K. Z. Fung, and M. H. Hon, *J. Ceram. Soc. Jpn.* **108,** 462 (2000).
13. Y. M. Hon, K. Z. Fung, and M. H. Hon, *J. Eur. Ceram. Soc.* **21,** 515 (2001).
14. T. Tsumura, A. Shimizu, and M. Inagaki, *J. Mater. Chem.* **3,** 995 (1993).
15. S. I. Pyun, Y. M. Choi, and I. D. Jeng, *J. Power Sources* **68,** 593 (1997).
16. W. Liu, G. C. Farrington, F. Chaput, and B. Dunn, *J. Electrochem. Soc.* **143,** 879 (1996).
17. M. Arima, M. Kakihana, Y. Nakamura, M. Yashima, and M. Yoshimura, *J. Am. Ceram. Soc.* **79,** 2847 (1996).
18. G. G. Amatucci, C. N. Schmutz, A. Blyr, C. Sigala, A. S. Gozdz, D. Larcher, and J. M. Tarascon, *J. Power Sources* **69,** 11 (1997).
19. Y. Gao and J. R. Dahn, *J. Electrochem. Soc.* **143,** 1783 (1996).
20. F. Le Cras, P. Strobel, and M. Anne, *Eur. J. Solid State Inorg. Chem.* **33,** 67 (1996).
21. R. J. Gummow, A. de Kock, and M. M. Thackeray, *Solid State Ionics* **69,** 59 (1994).
22. C. Masquelier, M. Tabuchi, K. Ado, R. Kanno, Y. Kobayashi, Y. Maki, O. Nakamura, and J. B. Goodenough, *J. Solid State Chem.* **123,** 255 (1996).
23. M. M. Thackeray, A. D. Kock, M. H. Rossouw, D. Liles, R. Bittihn, and D. Hoge, *J. Electrochem. Soc.* **139,** 363 (1992).
24. Y. K. Sun, K. H. Lee, S. I. Moon, and I. H. Oh, *Solid State Ionics* **112,** 237 (1998).
25. Y. Xia and M. Yoshio, *J. Power Sources* **66,** 129 (1997).
26. L. Hernan, J. Morales, L. Sanchez, and J. Santos, *Solid State Ionics* **104,** 205 (1997).
27. A. Yamada, K. Miura, K. Hinokuma, and M. Tanaka, *J. Electrochem. Soc.* **142,** 2149 (1995).